ISSN: 3007-9640 DOI: https://doi.org/10.70114/acmsr.2026.6.1.P52

Particle Assembly Based on Double-Sided Acoustic Holography

Najat Hussain[1,2], Yonghao Wen [1], Zonglin Li [1], Juan Zhou [1], Laixin Huang [1] *, Fei Li [1, 2] *

[1] Research Center for Advanced Detection Materials and Medical Imaging Devices, Shenzhen Institutes of Advanced Technology, Chinese Academy of Sciences, Shenzhen, 518055, China

[2] University of Chinese Academy of Sciences, Beijing 100049, China

Corresponding authors: huanglx@siat.ac.cn, fei.li@siat.ac.cn

Abstract. Acoustic holography (AH) has emerged as a powerful technique for non-invasive and contactless manipulation of microscopic objects, enabling precise spatial organization in bioassembly and tissue modeling. Compared with a single lens for only phase modulation, using two lenses provides phase and amplitude modulation in acoustic field control, resulting in higher quality holographic images. However, dual-lens configurations suffer from acoustic refraction effects and therefore require precise positional calibration during experiments. Here, we present an improved holographic acoustic tweezer (HAT) system that integrates two holographic lenses into a single double-sided acoustic lens by introducing an impedance-matched buffer layer between them. This configuration eliminates refraction-induced alignment errors while enabling effective microparticle assembly through precise control of the acoustic field. Our method provides a solid foundational platform for sustained in vitro manipulation of cells, with potential applications in modeling disease mechanisms, evaluating therapeutic responses, advancing regenerative medicine, and organ modeling.

Keywords: Acoustic tweezers; Acoustic holography; Bioassembly; Acoustic radiation force; Particle manipulation

1. Introduction

The precise spatial organization of biological building blocks is a fundamental challenge in tissue engineering, regenerative medicine, and organ modeling [1, 2]. Building such tissue-like architectures in vitro requires tools that can manipulate delicate biological or biomimetic particles with high spatial accuracy and minimal disturbance. While conventional techniques such as scaffold-based assembly (supportive structures for cell growth), microfluidics (control of fluids on a microscopic scale), and 3D bioprinting [3] have improved biofabrication, they often suffer from limited resolution, involve invasive procedures, time-consuming, and lack flexibility for dynamic, reconfigurable patterning. Consequently, contactless and highly controllable bioassembly strategies have emerged. Among these, acoustic tweezers (AT)—devices that use sound waves to move or trap small objects—show great potential for non-invasive, contactless, fast, and precise manipulation of micro- and nanoscale objects [4]. By generating acoustic radiation force (ARF), these tweezers trap, move, and arrange particles or cells without physical contact, thereby preserving their viability and structure.

Conventional acoustic tweezers are often limited to single-particle or simple two-dimensional manipulations, and restricts their application for complex tissue-scale assembly [5]. To address these limitations, acoustic holography-based tweezers have been developed. They use holographically shaped acoustic wavefronts to create 2D or 3D trapping landscapes that can be reconfigured [6] . This approach allows for precise and dynamic positioning of multiple particles simultaneously. It also enables arbitrary spatial arrangements, making it suitable for constructing organ-scale biomimetic architectures.

Traditional AH systems use multiple algorithms to design a single phase lens to generate the target sound field [4, 7]. In contrast, using two lenses provides additional degrees of freedom to

ISSN: 3007-9640 DOI: https://doi.org/10.70114/acmsr.2026.6.1.P52
modulate both phase and amplitude in acoustic field control and generates higher quality holographic images [8, 9]. However, dual-lens configurations suffer from acoustic refraction effects at the interface between separate lenses, requiring precise positional calibration during applications [9], and the two lenses also increase the device complexity, resulting in alignment errors and a loss of positioning accuracy.

In this study, we employed an improved holographic acoustic tweezer (HAT) system based on an integrated double-sided acoustic lens with an impedance-matched buffer layer. This design eliminates refraction-induced misalignment and simplifies experimental calibration while maintaining precise wavefront control. We demonstrate that the lens can synthesize complex acoustic fields with high fidelity and successfully achieve programmable patterning of microbubbles (SonoVue®) into predefined structures [10, 11]. These findings confirm the feasibility of our approach for reliable, stable, and high-quality acoustic bioassembly

2. Materials and Methods

2.1 Working Principle of HAT

The acoustic holographic lens transforms an incident plane wave into a tailored acoustic field through controlled phase modulation. Our design positions the imaging plane 14 mm from holographic plane 1 and 7 mm from holographic plane 2. We employ a single-iteration calculation strategy [12] rather than iterative approaches to ensure consistent axial morphology, enabling precise sound field synthesis [12, 13]. The binarized target image shown in Fig. 1(a) was propagated using the angular spectrum method (ASM) to obtain phase distributions for both holographic planes Fig. 1(b) and Fig. 1(c).

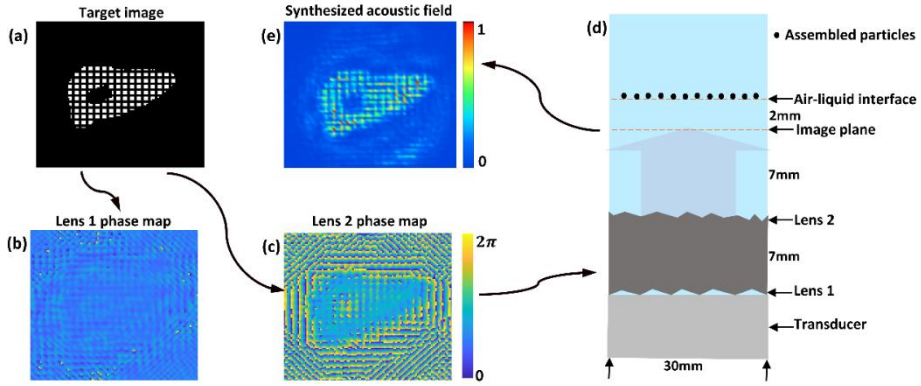


Fig.1. Double-sided acoustic holographic lens and the principles of their use in assembling microparticle. (a) The target image is back-propagated from the imaging plane to the holographic plane 1 and forward-propagated from the holographic plane 1 to the imaging plane using the angular spectrum method. (b-c) Phase distribution of Lens 1 and Lens 2. (d) Workflow diagram of HAT. (e) Synthesized acoustic field captured by hydrophone in the imaging plane.

The design process of double-sided acoustic holographic lens consists of four steps.

Step I: The grayscale target image was converted to binary dot-matrix form. The desired image field $A_{0,1}e^{i\varphi_{0,1}}$ is back-propagated from the imaging plane to holographic plane 2, producing acoustic field distribution $A_{2,1}e^{i\varphi_{2,1}}$ with target phase initialized as $\varphi_{0,1} = 0$

Step II: Field distribution $A_{2,2}e^{i\varphi_{2,2}}$ at holographic plane 2 is back-propagated to holographic plane 1, generating field $A_{1,2}e^{i\varphi_{1,2}}$. The amplitude remains unchanged: $A_{2,2} = A_{2,1}$, while phase resets to zero ($\varphi_{2,2} = 0$).

Step III: Field $A_{1,3}e^{i\varphi_{1,3}}$ at holographic plane 1 is forward-propagated to holographic plane 2, yielding $A_{2,3}e^{i\varphi_{2,3}}$. The amplitude $A_{1,3}$ and phase $\varphi_{1,3}$ correspond to the incident plane wave amplitude A_{in} and phase $\varphi_{1,2}$.

ISSN: 3007-9640 DOI: https://doi.org/10.70114/acmsr.2026.6.1.P52

Step IV: Field $A_{2,4}e^{i\varphi_{2,4}}$ at holographic plane 2 is propagated forward to the imaging plane, producing reconstructed field $A_{0,4}e^{i\varphi_{0,4}}$. The amplitude $A_{2,4}$ and phase $\varphi_{2,4}$ are set to $A_{2,3}$ and $\varphi_{2,1}$, respectively.

Wave propagation is calculated using the angular spectrum method (ASM):

$$P(x,y,z) = \mathrm{F}^{-1}\left(\mathrm{F}\left(P_{in}(x,y,z=0)\right) \bullet H\left(k_x,k_y,z\right)\right) \quad (1)$$

where $H\left(k_x,k_y,z\right) = e^{-iz\sqrt{k^2-k_x^2-k_y^2}}$ is the propagation kernel, $\mathrm{k} = \frac{\omega}{c_m}$ is the wave number in the medium (water), ω the angular frequency, c_m the sound speed in the liquid medium, and (k_x,k_y) the transverse spatial frequencies. Symbols F and F^{-1} denote the Fourier and inverse Fourier transform, respectively. Forward propagation applies when $z>0$ and backward when $z<0$. Equation (1) describes how an acoustic plane wave propagates between planes.

To suppress spatial aliasing, a low-pass filter attenuates high spatial frequency components. The critical cutoff wave number k_c is determined in reference [7]:

$$k_c = k\sqrt{\frac{D^2/2}{\frac{D^2}{2}+z^2}} \quad (2)$$

where D denotes the transverse dimension of the computational domain. Equation (2) shows that the filter enforces H = 0 for all spatial frequency components that satisfy $\sqrt{k_x^2+k_y^2} > k_c$, effectively preventing spurious high-frequency contributions from contaminating the propagated field. Under thin lens approximation, the relative thickness distribution ΔT is determined from the phase modulation $\Delta\varphi$ using one-dimensional transmission line theory [8, 14, 15].

$$\Delta T = \frac{\Delta\varphi}{k_m - k_h} \quad (3)$$

Where k_m and k_h denote the wave numbers of the medium (water) and the holographic lens material (red wax) respectively.

2.2 Acoustic field simulation and measurement

In this study, we used the k-wave MATLAB toolbox [16] for three-dimensional acoustic field calculations with a speed-of-sound contrast ratio of 1.55.

Assuming a non-reflective medium, we set the grid dimensions of the computational domain to $x \times y \times z = 30\ \text{mm} \times 30\ \text{mm} \times 30\ \text{mm}$ with spacing $\frac{1}{6}\lambda\ (\lambda = 0.65\ \text{mm})$. Operating frequency was $f = 2.25\ \text{MHz}$ with a source amplitude 0.5×10^6. Material parameters were as follows: the red wax lens ($\rho_h = 1352\ \text{kg/m}^3$, $c_h = 2326\ \text{m/s}$), and the water medium ($\rho_m = 1000\ \text{kg/m}^3$, $c_m = 1500\ \text{m/s}$). Symbols ρ_h, c_h, ρ_m, c_m denote the density, sound speed of hologram lens and medium, respectively.

For acoustic field measurement, a piezoelectric transducer with a central frequency of 2.25 MHz was driven by a waveform generator (DG4062, RIGOL) via a power amplifier (LZY-22, Mini-Circuits) to emit acoustic beams through a lens immersed in water. These were detected by a calibrated 0.2 mm hydrophone (NH0200, Precision Acoustics) with signals recorded on a digital oscilloscope as shown in Fig.2.

ISSN: 3007-9640 DOI: https://doi.org/10.70114/acmsr.2026.6.1.P52

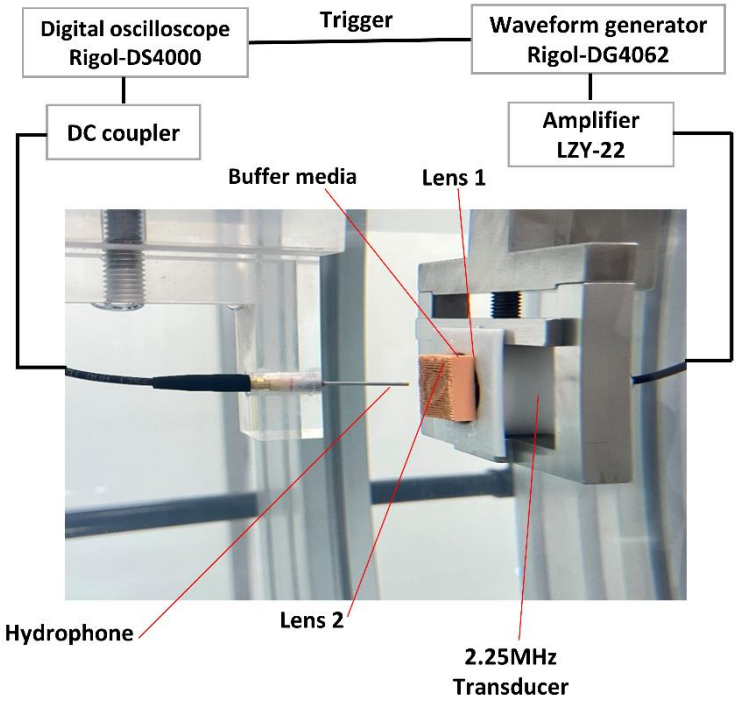


Fig.2. Experimental setup for synthesizing acoustic measured pressure

2.3 Quantification of ARF on particles

In acoustic fields, acoustic radiation force (ARF) is the primary mechanism governing the motion of particles. When the particle size is much smaller than the wavelength, ARF is governed by Gor'kov's formulation [17].

$$F_R = -\nabla U \tag{4}$$

$$U = 2\pi r^3 \rho_m \left(\frac{p_1^2}{3\rho_m^2 c_m^2} f1 - \frac{u_1^2}{2} f_2 \right) \tag{5}$$

where $f_1 = 1 - \frac{c_m^2 \rho_m}{c_p^2 \rho_p}$ and $f_2 = 2\frac{\rho_p - \rho_m}{2\rho_p + \rho_m}$. Here, u_1 and p_1 denote the first-order particle velocity and acoustic pressure of the surrounding medium, r is the particle radius , while ρ_m and c_m represent the medium's density and sound speed.

In this study, we manipulated microbubbles (SonoVue®) by ultrasound (US). The material parameters are: density $(\rho_p) = 120\ \mathrm{kg/m^3}$, acoustic speed $(c_p) = 733\ \mathrm{m/s}$, and radius $(r) = 2.5\ \mu\mathrm{m}$. For the medium, $\rho_m = 1000\ \mathrm{kg/m^3}$ and $c_m = 1500\ \mathrm{m/s}$.

2.4 Experimental setup for particle manipulation

The experimental setup for particle manipulation comprises an ultrasound transducer integrated with a 3D-printed acoustic lens beneath a water-filled Petri dish. The lens modulates the incident acoustic field to generate the target pressure distribution. The particle suspension undergoes acoustic manipulation and assembles into predefined patterns. The configuration is immersed in a water tank to maintain acoustic coupling and minimize distortions. A digital camera positioned above captures real-time particle patterning for visualization and documentation. A schematic model is shown in Fig.1(d).

3. Results and discussion

The three-dimensional simulated and experimentally measured acoustic fields are presented comprehensively in Fig. 3. The simulated normalized pressure field in the xy-plane is displayed in Fig. 3(a), with a magnified view of the region of interest provided in Fig. 3(b). To demonstrate the

ISSN: 3007-9640 DOI: https://doi.org/10.70114/acmsr.2026.6.1.P52
trapping mechanism, the normalized ARF for a microparticle is shown in Fig. 3(c), indicating force directions that guide particles toward trapping positions. The three-dimensional beam propagation and axial focusing characteristics are further illustrated through maximum pressure field distributions in the xz-plane and yz-plane, as presented in Fig. 3(d) and Fig. 3(e), respectively. The experimentally measured acoustic field in the imaging plane is captured in Fig. 3(f), showing excellent agreement with the simulated pattern in Fig. 3(b), thereby validating the successful implementation of the acoustic holographic design.

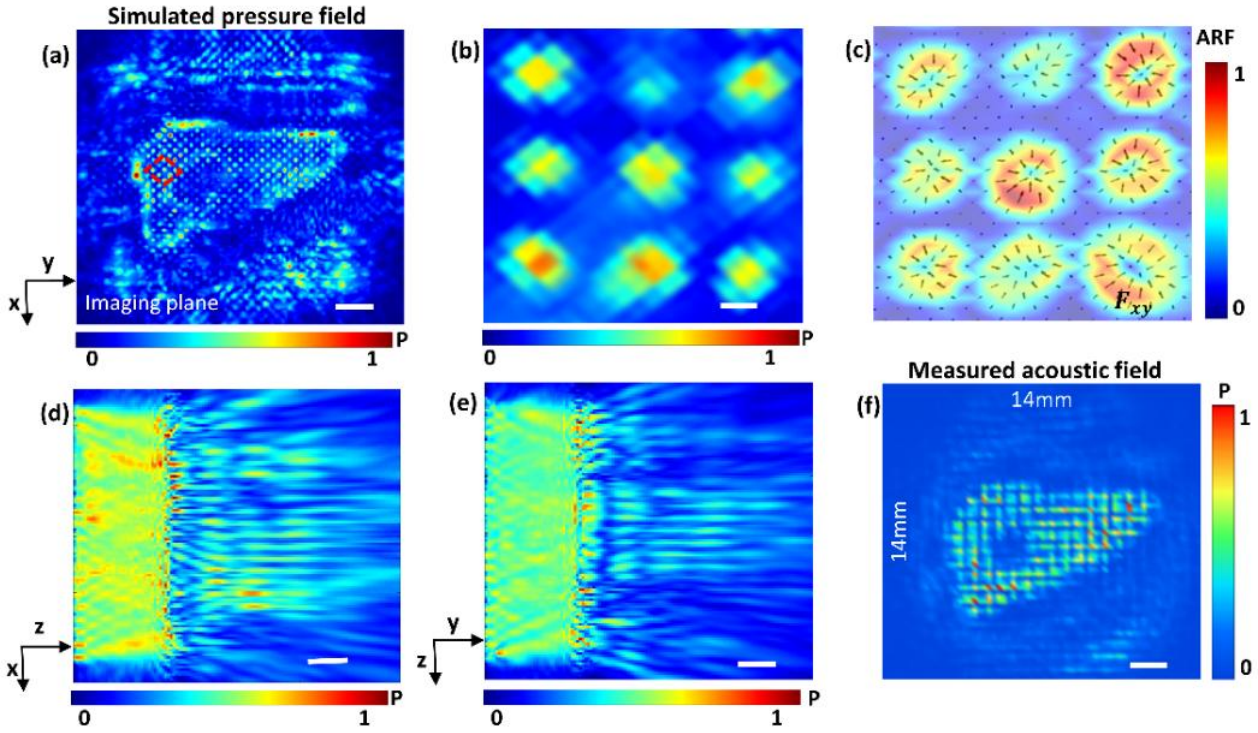


Fig. 3. 3D simulation and experimentally measured pressure. (a) Simulated pressure field in the xy-plane. (b) Inset: zoom-in view of the region of interest (ROI) in a red dashed box. Scale bar: 500 μm. All scale bars other than the inset are 5 mm. (c) A normalize ARF f_{xy} for a 5 μm diameter SonoVue® bubble particle. (d-e) Maximum pressure field in the xz and yz planes respectively. (f) Measured acoustic field in the image plane by hydrophone.

Compared with previously reported dual-lens acoustic holography systems that require precise positional calibration and suffer from refraction at lens interfaces, the integrated lens configuration significantly improves field fidelity while simplifying experimental alignment. Although minor attenuation due to lens thickness was observed, it did not compromise the formation of complex target fields.

The close agreement between the simulated and measured acoustic fields, as shown in Fig. 3(a) and Fig. 3(f) validates the effectiveness of our integrated lens design.

Fig. 4 demonstrates the acoustic manipulation capability of our method. With US OFF (Fig. 4(a)), microbubbles exhibit random dispersion due to Brownian motion and gravity [18]. Upon ultrasound activation at 2.25 MHz (Fig. 4(b)), acoustic radiation forces drive microbubbles toward pressure nodes, forming a well-defined pattern that matches the designed holographic structure. The transformation from random to organized distribution demonstrates precise controllability for on-demand microparticle patterning.

ISSN: 3007-9640 DOI: https://doi.org/10.70114/acmsr.2026.6.1.P52

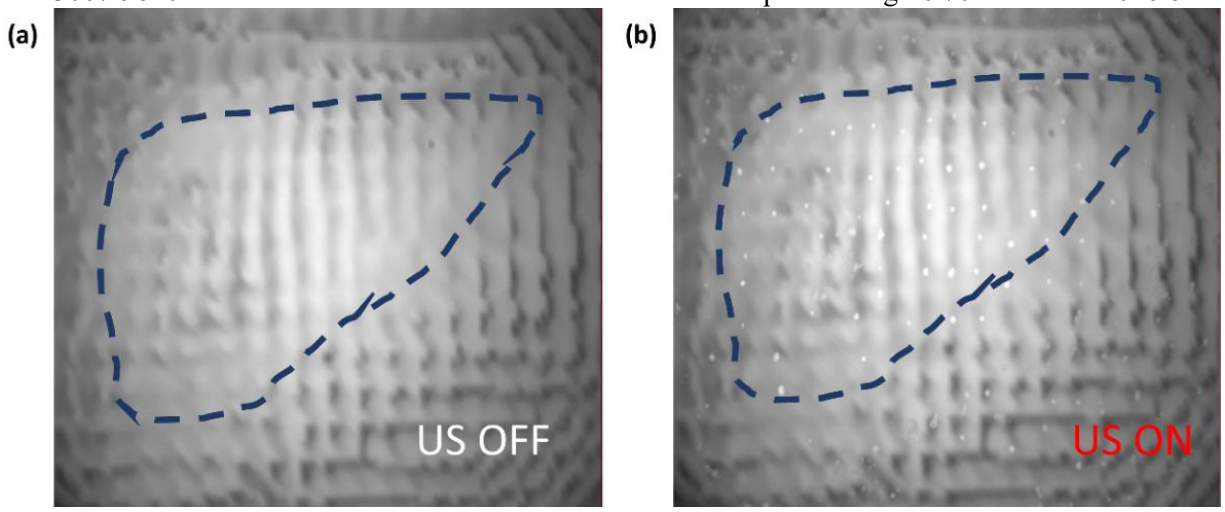


Fig.4. Acoustic patterning of microbubbles by double-sided acoustic hologram lens. (a) Random particle distribution with ultrasound (US) OFF. (b) Organized particle assembly at acoustic pressure nodes when US is ON.

4. Conclusion

We presented an integrated holographic acoustic tweezer system for contactless and programmable particle assembly using a single impedance-matched, double-sided acoustic lens. The proposed design suppresses refraction and alignment errors inherent to conventional dual-lens systems, resulting in improved acoustic field fidelity. Simulations and experiments show strong agreement, demonstrating stable assembly of microbubbles into predefined patterns. Our method provides a strong foundation for advancing toward bioassembly applications.

5. Acknowledgement

This work was supported by National Natural Science Foundation of China (Grant Nos. 82427804), Shenzhen Science and Technology Program (Grant No. JCYJ20241202124806009) and Key Laboratory for Magnetic Resonance and Multimodality Imaging of Guangdong Province (Grant No. 2023B1212060052).

References

[1] Rasekh, M., M.S. Arshad, and Z. Ahmad, Advances in Drug Delivery Integrated with Regenerative Medicine: Innovations, Challenges, and Future Frontiers. Pharmaceutics, 2025. 17(4): p. 456.

[2] Akhtar, Z., Exploring biomedical engineering (BME): Advances within accelerated computing and regenerative medicine for a computational and medical science perspective exploration analysis. Journal of Emergency Medicine, 2024. 2: p. 1-23.

[3] Barua, R., et al., Recent advances in the fabrication of vascularized tissues and blood vessels: A state-of-the-art review. Physics of Fluids, 2025. 37(10).

[4] Yang, S., et al., Acoustic tweezers for advancing precision biology and medicine. Nature Reviews Methods Primers, 2025. 5(1): p. 49.

[5] Morrell, M.C., J.E. Lee, and D.G. Grier, Spectral holographic trapping: Creating dynamic force landscapes with polyphonic waves. Physical Review E, 2024. 109(4): p. 044901.

[6] Guo, Y., et al., Porous Granular Hydrogel Scaffolds Biofabricated from Dual-crosslinked Hydrogel Microparticles for Breast Tissue Engineering. Materials Today Bio, 2025: p. 102006.

[7] Melde, K., et al., Holograms for acoustics. Nature, 2016. 537(7621): p. 518-522.

[8] Li, C., et al., Acoustic-holography-patterned primary hepatocytes possess liver functions. Biomaterials, 2024. 311: p. 122691.

ISSN: 3007-9640 DOI: https://doi.org/10.70114/acmsr.2026.6.1.P52
[9] Brown, M.D., Phase and amplitude modulation with acoustic holograms. Applied Physics Letters, 2019. 115(5).

[10] Alsadiq, H. and Z. Alhay, Mechanical Properties of Medical Microbubbles and Echogenic Liposomes—A Review. Micromachines, 2025. 16(5): p. 588.

[11] Gu, Y., et al., Acoustofluidic holography for micro-to nanoscale particle manipulation. ACS nano, 2020. 14(11): p. 14635-14645.

[12] Ma, Z., et al., Acoustic holographic cell patterning in a biocompatible hydrogel. Advanced Materials, 2020. 32(4): p. 1904181.

[13] Zeng, X. and R.J. McGough, Evaluation of the angular spectrum approach for simulations of near-field pressures. The Journal of the Acoustical Society of America, 2008. 123(1): p. 68-76.

[14] Lin, X., et al., All-optical machine learning using diffractive deep neural networks. Science, 2018. 361(6406): p. 1004-1008.

[15] Menakath, M.M., et al., Experimental Validation of Underwater Target Modeling Using K-Wave Toolbox for Acoustical Imaging. IEEE Sensors Letters, 2025.

[16] Masud, A.A. and J. Liu, Numerical simulation of impulse-induced surface acoustic waves for elastography purposes using k-Wave simulation toolbox. Journal of Applied Physics, 2024. 136(16).

[17] Xu, X., et al., Unveiling the frequency-dependent dynamics of acoustic radiation force on lipid-coated ultrasound bubbles. Physics of Fluids, 2025. 37(8).

[18] Muñoz-Gil, G., et al., Quantitative evaluation of methods to analyze motion changes in single-particle experiments. Nature Communications, 2025. 16(1): p. 6749.